Image deconvolution research: its scope and importance in live cell microscopy

Muthuvel Arigovindan*

Department of Electrical Engineering, Indian Institute of Science, Bangalore 560 012, India

Fluorescence microscopy has become an indispensable tool in cell biology research due its exceptional specificity and ability to visualize subcellular structures with high contrast. It has highest impact when applied in 4D mode, i.e. when applied to record 3D image information as a function of time, since it allows the study of dynamic cellular processes in their native environment. The main issue in 4D fluorescence microscopy is that the phototoxic effect of fluorescence excitation gets accumulated during 4D image acquisition to the extent that normal cell functions are altered. Hence to avoid the alteration of normal cell functioning, it is required to minimize the excitation dose used for individual 2D images constituting a 4D image. Consequently, the noise level becomes very high degrading the resolution. According to the current status of technology, there is a minimum required excitation dose to ensure a resolution that is adequate for biological investigations. This minimum is sufficient to damage light-sensitive cells such as yeast if 4D imaging is performed for an extended period of time, for example, imaging for a complete cell cycle. Nevertheless, our recently developed deconvolution method resolves this conflict forming an enabling technology for visualization of dynamical processes of light-sensitive cells for durations longer than ever without perturbing normal cell functioning. The main goal of this article is to emphasize that there are still possibilities for enabling newer kinds of experiment in cell biology research involving even longer 4D imaging, by only improving deconvolution methods without any new optical technologies.

Keywords: Cell biology, fluorescence microscopy, image deconvolution, phototoxic effect.

Introduction

LIGHT microscopy has made profound impact in cell biology research due to the fact that it allows imaging cells without any sample preparation steps that might cause the death of the cells. Among all known light microscopy methods, fluorescence microscopy has become the most preferred live cell imaging method because of its ability to visualize specific subcellular structures with high contrast. In fluorescence microscopy, the targeted subcellular structure is infused with the fluorescence substance known as a fluorophore and is kept under the fluorescence microscope. The fluorescence microscope is composed of a subsystem for launching excitation light into the cell and a subsystem for detecting the light emitted by the fluorophores. The excitation subsystem illuminates the cell with light of appropriate wavelength which is absorbed by the fluorophores. The fluorophores, as a response to the excitation, emit light of higher wavelength which is collected by the detection subsystems and its intensity is measured.

The detection subsystem typically measures a 3D intensity image that quantifies the spatial distribution of fluorophore concentration that represents a targeted subcellular structure. This 3D acquisition is performed in either of two ways: as a set of point measurements where each point measurement is obtained by scanning the volume of interest along three axes, or as a set of 2D image measurements that is obtained by scanning the system along the depth axis. A 4D image acquisition, which is the focus of this article, amounts to recording a series of 3D images for a set of regular time intervals.

When fluorescence microscopy is performed in 4D mode, it allows the study of dynamic cellular processes, which is one of the most important facets of cell biology research. When the time sampling is sufficiently dense, analysis of 4D microscopic images allows spatio-temporal localization of key events in dynamic cellular processes. Examples of processes studied using 4D microscopy include mitosis[1], meiosis[2], cytokinesis[3], nuclear envelope breakdown[4], nuclear envelope reassembly[5], endocytosis[6], etc. When imaging is performed at multiple wavelengths by labelling different organelles using fluorophores with different emission wavelengths, 4D imaging will reveal complex spatial and temporal relationships among different organelles during a cellular process.

The most important parameter in fluorescence microscopy is the excitation dose used for a basic measurement (either a point measurement or 2D image measurement), which is the product of intensity of illuminating light and duration of exposure to the illumination. This excitation dose determines the signal-to-noise ratio (SNR) of the measured images, and specifically, the SNR is directly proportional to the excitation dose. This suggest that it is required to keep the excitation dose as high as possible. On the other hand, excitation dose leads to alteration of

*e-mail: mvel@ee.iisc.ernet.in

normal cell functioning due to the toxic effect of excited fluorophores, which we will call phototoxicity. The severity of phototoxicity is directly proportional to the dose level. This dictates that the excitation dose level should be kept as low as possible. This limitation is more stringent in 4D imaging since it requires exposure for an extended period of time and damaging effect of excitation dose gets accumulated over the imaging period. Hence the excitation dose used for a basic measurement should be kept low. This will lead to high level of noise causing a severe loss of resolution.

The first goal of this article is to indicate that this conflict, according to the current status of published technology except our recently developed one, leads to the failure of 4D microscopy in studying light sensitive cells such as yeasts. The second goal is to show, by elaborating a break-through we obtained recently[7], how a carefully designed deconvolution method can rescue 4D microscopy from this failure. The third goal is to demonstrate that there are still possibilities to improve the deconvolution methods further so as to widen the applicability of 4D fluorescence microscopy in cell biology research.

An overview of fluorescence microscopy

In fluorescence microscopy, to visualize a specific subcellular organelle, it is required to infuse an appropriate fluorophore with the target organelle. The fluorophore in this context is known as the marker and the infusion process is known as labelling. There are mainly two types of labelling, namely immunolabelling and labelling by fluorescent protein. In the first type of labelling, to visualize an organelle composed of a specific type of protein (target protein), another type of protein molecules known as antibodies that are specifically constructed for the target proteins are attached with a certain type of dye molecules having fluorescence property. When these antibodies are injected into the cell, they attach to the target protein molecules, thereby fluorescently 'painting' the target organelle. In the second type of labelling, given a target organelle composed of a target protein, the gene corresponding to the target protein is first identified in the organism. Then the gene is modified such that, whenever the cell produces the target protein, another protein having fluorescent property is also produced together forming a complex with the target protein. This also effectively leads to 'painting' of the target organelle with fluorescence property. Both types of labelling methods have their own merits and demerits.

With target subcellular structure appropriately labelled, the task of microscopy is to measure the concentration of the fluorophore as a 3D spatial distribution. Depending on the measurement scheme, fluorescence microscopes can be broadly classified into two types: Widefield microscopes and confocal microscopes. In a widefield microscope, a basic measurement is a 2D image of the intensity distribution of the emission wavefront coming

through the detection subsystem. This 2D image contains spatial information about the target subcellular structures in the form of the concentration of the fluorophore, mainly from the plane on which the detection subsystem is focused. Hence a 3D image measurement is done by recording 2D images by scanning the focal plane across depth covering the sample volume of interest. In a confocal microscope, a basic measurement is the concentration of fluorophores in a small sample volume that is considered as a point measurement. Hence a 3D image acquisition involves scanning along three directions. In the following we will first describe the widefield system and then the confocal system.

There are a class of microscopes known as super-resolution microscopes that achieve resolution beyond theoretical resolution limit of widefield and confocal microscopes by employing a variety of optical and chemical techniques. They are typically slow and incur high excitation dose. We do not consider super-resolution microscopes here, since according to the current status of the technology, they are not practicable for 4D imaging mainly because they incur high excitation dose.

The widefield microscope

Figure 1 provides a schematic representation of a widefield microscope. The illumination sub-system is composed of three lenses, namely the collimator lens CL, the tube lens TL′ and the objective lens. Lenses are characterized by the so-called focal planes which are the imaginary planes identified on both sides. Typically, when a wavefront travels from one focal plane to another through the lens, it becomes its own Fourier transform. P_F and P_{BF} are the front focal and back focal planes of the objective lens respectively. The front focal plane of TL′ coincides with P_{BF} and its back focal plane is P'_{IM}. The back focal plane of CL coincides with P'_{IM}, and its front focal plane is where the fibre end-face, which acts as point illumination
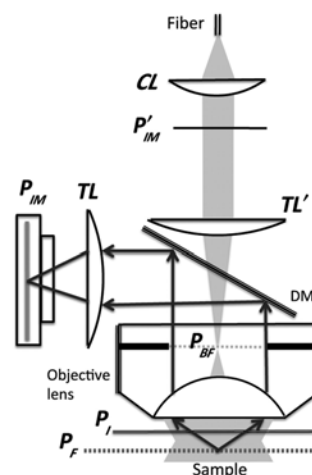

Figure 1. Schematic of a widefield microscope.

source, is located. This point source is mapped onto the plane P_{BF} again as a point source and this gets Fourier transformed to become uniform illumination intensity in the region below the objective lens.

The imaging specimen is mounted on a piece of glass known as coverslip (denoted by P_I in Figure 1) and placed under the objective lens. The space between the objective lens and coverslip is filled with glycerol, whose refractive index is the same as that of glass. There are two interfaces: the interface between the glycerol and the upper boundary of the coverslip, which will call the immersion interface, and the interface between the medium that holds the specimen and lower boundary of the coverslip, which we will call the mounting interface. Here all the components are immovable, except the coverslip which can move vertically in a controlled manner. Moving the coverslip vertically allows changing the cross-sectional part of the specimen that is cut by P_F.

As response to the uniform illumination, the labelled structure or organelle fluoresces with a higher wavelength which is collected by the detection subsystem. The detection subsystem is composed of the objective lens, tube lens TL and the camera whose image plane coincides with the plane P_{IM}. The fluorescence light travels upwards which is collected by the objective lens and reflected horizontally by the dichroic mirror DM. The reflected light is projected by the tube lens TL into the plane P_{IM}, which is measured by the camera. The role of the dichroic mirror is to reflect the emission light only without disturbing the path of the illumination light, which is achieved by exploiting the difference in the wavelengths. In simplified terms, the objective lens at P_{BF} generates a demagnified Fourier transform of the fluorescence amplitude distribution from P_F. This amplitude distribution is transformed again by the tube lens TL such that the amplitude distribution at P_{IM} is a magnified version of the amplitude distribution at P_F. The squared modulus of this amplitude distribution (intensity) is measured by the image sensor at P_{IM} as a 2D digital image. A 3D acquisition involves measuring a series of 2D images by scanning the coverslip such that P_F samples the required specimen volume with an appropriate step size.

In reality, each 2D image measured will also contain a sum of blurred versions of the intensity distribution from planes other than P_F, and hence the 3D measured image is not a quantitative representation of the target structure. However, this deviation can be modelled. Specifically, the wavefront incident on the image sensor can be related to the wavefront emitted from the target structure as a convolution expressed below:

$$R_a(x, y, z) = h_a(x, y, z) \oplus S_a(x, y, z)$$

$$= \int_{x', y', z'} h_a(x-x', y-y', z-z')S_a(x', y', z')\mathrm{d}x'\mathrm{d}y'\mathrm{d}z', \quad (1)$$

where $R_a(x, y, z)$ is the amplitude of the wavefront incident on the image sensor $S_a(x, y, z)$ is the wavefront emit-

ted from the target structure, and $h_a(x, y, z)$ is the amplitude point spread function (PSF) with the symbol $\oplus$ representing the convolution operation. The amplitude PSF represents the wavefront incident on the image sensor when the specimen is replaced by a fluorescence point source. An image sensor actually measures the intensity of the wavefront (squared modulus of the wavefront amplitude). If $R(x, y, z)$ is the measured image, then $R(x, y, z) = |R_a(x, y, z)|^2$. Hence to express the measured intensity image in terms of target emission intensity, one needs to compute the squared modulus of eq. (1) which is likely to give nonlinear relations. Remarkably, by using the so-called property of incoherence of the wavefronts involved, and also the fact that an image detector measures only the intensity averaged over an finite duration (few milliseconds), it can be shown that the measured intensity also satisfies the following linear relation

$$R(x, y, z) = h(x, y, z) \oplus S(x, y, z), \quad (2)$$

where $S(x, y, z) = |S_a(x, y, z)|^2$ and $h(x, y, z)$ is the intensity PSF given by $h(x, y, z) = |h_a(x, y, z)|^2$. The intensity PSF can be measured experimentally by placing a fluorescence bead under the objective lens and can also be computed numerically from the mathematical expression of the theoretical amplitude PSF. The Fourier transform of the intensity PSF is known as the intensity optical transfer function (OTF). It is well known that if $\hat{R}(X, Y, Z)$ and $\hat{S}(X, Y, Z)$ are the Fourier transforms of $R(x, y, z)$ and $S(x, y, z)$ respectively, then they are related as $\hat{R}(X, Y, Z) = H(X, Y, Z) \hat{S}(X, Y, Z)$, where $H(X, Y, Z)$ is the intensity OTF.

Figure 2 a displays the mid xz section of the theoretical intensity PSF of a widefield microscope and Figure 2 b displays the mid xz section of the absolute value of its Fourier transform (intensity OTF). Theoretical PSF and its Fourier transform are rotationally symmetric in the xy plane and hence these visualizations provide the complete information. This symmetry is approximately exhibited by the experimental PSFs as well. If this symmetry is taken into account, we observe another property: each 2D section has a form of concentric circle with maximum radius increasing as the axial distance increases. Also, it can be observed that the intensity summed over any 2D plane is independent of axial distance from the centre. This property manifests itself in the intensity OTF as the so-called missing cone. The term 'missing cone' denotes the zeros presents in two conical regions whose axes are aligned to the z-axis and whose vertices meet at the origin. The missing cone property stems from the fact that, in widefield imaging, planes in target structure corresponding to different values of z are discriminated by focal shifts. By the very nature of wave propagation in homogenous medium, this focal shift affects only high lateral (xy) Fourier frequencies.

Two important quantities that have been marked in Figure 2 b are the lateral cut-off frequency f_x and the axial cut-off frequency f_z. These are the highest Fourier

frequencies that can be passed by a microscope. Specifically, if $\hat{R}(X, Y, Z)$ is the Fourier transform of the measured image, then $\hat{R}(X, Y, Z) = 0$ for all X and Y satisfying certain conditions. Specifically, we have

$$\hat{R}(X, Y, Z) = 0, \text{ for all } X, Y, \text{ such that}$$
$$X^2 + Y^2 > 2\text{NA}/\lambda, \tag{3}$$

$$\hat{R}(X, Y, Z) = 0, \text{ for all } Z, \text{ such that}$$
$$Z > (n/\lambda)\left[1 - \sqrt{1 - (\text{NA}/n)^2}\right], \tag{4}$$

where NA is the so-called numerical aperture of the objective lens and n is the refractive index of the immersion medium.

Due to the missing cone in the OTF, the images measured by a widefield microscope have a characteristic appearance. In each 2D image section, signals from all other 2D sections of the target structure corresponding to low Fourier frequencies are visible. This makes the widefield images difficult to interpret. Fortunately, this problem can be overcome by deconvolution which attempts to invert the effect of operating the microscopes' transfer function on the target structure. This gives images of better resolution and also partially retrieves the frequencies lost in the missing cone region. Owing to the importance of deconvolution, widefield microscopy is always used in conjunction with deconvolution.

The confocal microscope

Confocal microscopy provides an alternative way to deal with the problem of the missing cone. In the following, we will present the schematic of a confocal microscope as

a modification of a widefield microscope. Figure 3 gives a schematic of a confocal microscope as a simple modification of the widefield microscope given in Figure 1. The new illumination subsystem is obtained by simply removing CL and placing a point source at the plane P'_{IM}, whereas the new detection subsystem is obtained by removing the camera and placing a point detector. The purpose of this schematic is only to facilitate understanding the working principle and a practical implementation will differ significantly. To understand the working principle, we first note that a point source in the plane P'_{IM} located at (x_0, y_0) gives an illumination pattern that is identical to the widefield intensity PSF, $h(x, y, z)$, located at $(x_0/M, y_0/M)$ in the specimen, where M is the magnification factor. This illuminates a small volume around the point $(x_0/M, y_0/M)$ and the fluorescence light emitted by this volume gets focused at the point (x_0, y_0) in the plane P_{IM}, which is detected by the point detector. Essentially, the intensity measured by the point detector is approximately the fluorophore concentration at the point $(x_0/M, y_0/M)$ in the specimen. A 2D image acquisition is done by scanning the point source and point detector in unison to cover the entire planes (P_{IM} and P'_{IM}), and 3D acquisition amounts to scanning P_{I} as well. As in the case of widefield imaging, the actual image (the target structure) and the measured image are related by a convolution $R(x, y, z) = h_s(x, y, z) \oplus S(x, y, z)$, where h_s is the point spread function of the confocal microscope. The point spread function for the scheme in Figure 3 is given by the square of the widefield point spread function, i.e. $h_s(x, y, z) = h^2(x, y, z)$.

Figure 4 gives a schematic for practical implementation of the point source and the point detector in a confocal microscope. The dichroic mirror DM is removed from the path between the objective lens and the tube lens,
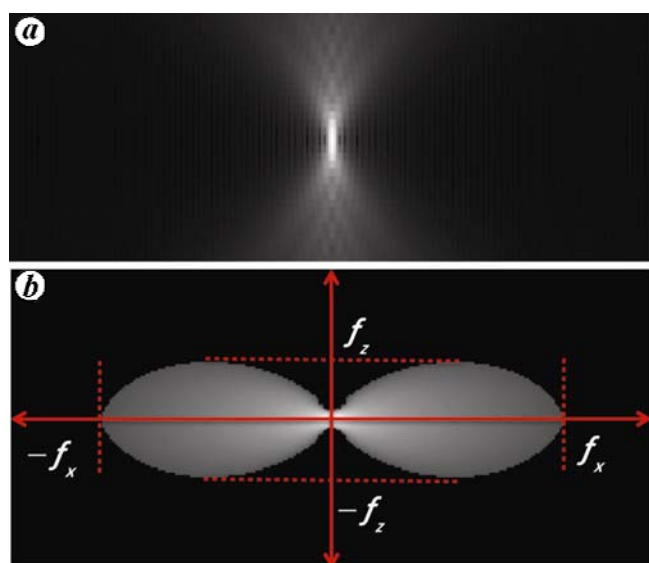
Figure 2. The transfer function of a widefield microscope. a, xz section of the PSF; b, xz section of the OTF.
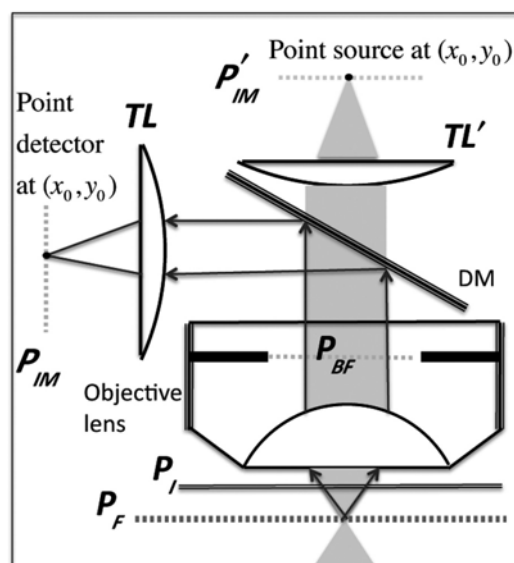
Figure 3. An ideal form of confocal microscope.

thereby eliminating the need for two tube lenses. A pinhole is placed at (x_0, y_0) in the plane P_{IM} and the dichroic mirror placed on top of the pinhole separates the illumination and detection light paths. Specifically, the uniform laser light incident on the focusing lens FL$'$ gets focussed onto the pinhole which acts as a virtual point source. This illuminates a small volume around the point $(x_0/M, y_0/M)$ in the specimen and the fluorescence light emitted by this volume gets focused at the pinhole. The emission light exiting the pinhole is reflected horizontally by the dichroic mirror and focused by the lens FL and then detected by the detector. The pinhole, dichroic mirror, the lens FL and detector together form a virtual point detector at (x_0, y_0) in the plane P_{IM}. In reality, the finite size of the pinhole should be taken into account in computing the actual PSF. The actual PSF of this type of set-up is given by $h_s(x, y, z) = [h(x, y, z) \oplus C(x, y)]^2$ where $C(x, y)$ is the image of the pinhole in the specimen space (circular aperture function). Note that a confocal PSF is approximately the square of a widefield PSF. Hence a confocal OTF is approximately the convolution of a widefield OTF with itself. Hence the missing cone problem is eliminated. Due to this reason, confocal microscopy has become a preferred technique for many researchers.

Confocal versus widefield microscope

Now we will compare the widefield microscope with the confocal microscope in terms of SNR and theoretical
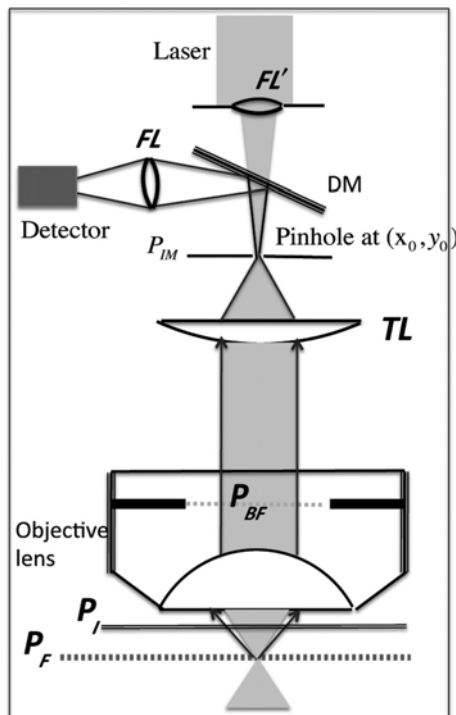

Figure 4. The confocal microscope.

resolution. Since the confocal OTF is a autocorrelation of a widefield OTF, the region in the Fourier space containing the frequencies passed by the confocal microscope is almost twice that of a widefield microscope. However, the relative gain for the Fourier frequencies that are additionally brought in by the confocal microscope is very low, and hence these additional frequencies will play a role in resolving the structural details only if noise is negligible. Unfortunately, this is condition is rarely met. Since the emission light is stopped by the pinhole in a confocal microscope, the images obtained from a confocal microscope have much lower SNR compared to those obtained from a widefield microscope. Hence the additional frequencies brought in by the confocal microscope become ineffective in resolving the structural details, except the frequencies near the vertices of the missing cone region. As a consequence, it turns out that the effective resolution of a confocal microscope becomes the same as that of a widefield microscope when the noise level is moderate. On the other hand, at high noise levels, the effective resolution of widefield microscope is significantly higher than a confocal microscope. Hence, in 4D imaging scenarios where dense time sampling is necessary, widefield microscopy performs better than the confocal microscopy. So we will limit our discussion to widefield microscopy in the remainder of this article.

An overview of deconvolution for widefield microscopy

The term 'deconvolution' refers to the task of inverting the convolution equation $R(x, y, z) = h(x, y, z) \oplus S(x, y, z)$ to obtain an estimate of the required 3D structure, $S(x, y, z)$ from the measured data, $R(x, y, z)$ with the constraint on the solution to be non-negative. The convolution equation $R(x, y, z) = h(x, y, z) \oplus S(x, y, z)$ in Fourier domain becomes $\hat{R}(X, Y, Z) = H(X, Y, Z)\hat{S}(X, Y, Z)$ and a straightforward way to compute the solution will be as follows:

$$\hat{S}_p(X, Y, Z) =$$

$$\begin{cases} \hat{R}(X, Y, Z)/H(X, Y, Z), & \text{if } |H(X, Y, Z)| \neq 0, \\ 0, & \text{Otherwise.} \end{cases} \quad (5)$$

If the noise level is negligible, the inverse Fourier transform of $\hat{S}_p(X, Y, Z)$, $S_p(x, y, z)$ will have an improved visibility of fine details when compared to the measured image $R(x, y, z)$.

There are two issues in the above approach: the solution will have negative values due to the loss of frequencies in the missing cone region; since the magnitude of $H(X, Y, Z)$ will be low at high frequencies, noise will be amplified due to division by $H(X, Y, Z)$. To circumvent these issues, an iterative approach was proposed[8]. Given an estimate of

the solution, $S^{(k)}$, the next improved estimate is computed as

$$S^{(k+1)}(x, y, z) = \mathcal{P}[S^{(k)}(x, y, z) + \gamma(R(x, y, z)$$
$$- h(x, y, z) * S^{(k)}(x, y, z))], \qquad (6)$$

where γ is a parameter that is heuristically chosen and $\mathcal{P}[\cdot]$ represents the processing steps involving smoothing for noise removal and clipping-off the negative value. The smoothing operation is typically done by convolving with a Gaussian function of appropriate width. This method avoids noise build-up and negative values in the solution. Interestingly, this method also retrieves part of the frequencies lost in the missing cone region as an effect of clipping the negative values.

The above method performs satisfactorily when the noise is low, i.e. when applied on images measured with high excitation dose. At higher noise levels, the Gaussian smoothing is required to be made stronger, which also leads to loss of image details. To handle higher noise levels, robust methods adopt a regularization approach, where the required solution is obtained as the maximizer of its probability of being the source of the measured image. Denoting the target structure by g and the measured image by f, this probability, which is known as the posteriori probability, is given by

$$p(g \mid f) = \frac{p(f \mid g)p(g)}{p(f)}, \qquad (7)$$

where $p(f|g)$ is the probability of obtaining the observation f given g and $p(g)$ is the probability distribution of g. $p(f)$ is the probability distribution of f. Since $p(f)$ is independent of the minimization variable g, it can be removed from the expression. $p(f|g)$ is the product of probabilities of obtaining $f(x, y, z)$ given the ideal measurement $h(x, y, z) * g(x, y, z)$ for all points (x, y, z), which is given by

$$p(f \mid g) = \prod_{x,y,z} p_n(f(x, y, z), (h * g)(x, y, z)),$$

where $p_n(f(x, y, z), (h * g)(x, y, z))$ is the density function that represents the random process generating the actual measured value from the expected value $(h * g)(x, y, z)$. The probability $p(g)$ is known as prior probability and is typically assumed to be of the form $p(g) = e^{-\lambda J(g)}$ where $J(g)$ is a measure quantifying the roughness of the image g. $J(g)$ is more commonly known as the regularization or roughness functional.

To maximize eq. (7), it is customary to minimize its negative logarithm of the product $p(f|g)p(g)$. This leads to the following minimization problem

$$g_{\text{opt}}(x, y, z) =$$
$$\arg\min_g \sum_{x,y,z} D(f(x, y, z), (h * g)(x, y, z)) + \lambda J(g), \quad (8)$$

where $D(R(x, y, z), (h * g)(x, y, z))$ is the pointwise distance measure that depends on the assumed probability density function $p_n(f(x, y, z), (h * g)(x, y, z))$. If Gaussian density function is assumed, then $D(f(x, y, z), (h * g) \times (x, y, z)) = (f(x, y, z) - (h * g)(x, y, z))^2/\sigma^2$, where σ^2 is the variance of the Gaussian process. If Poisson density function is assumed, then $D(f(x, y, z), (h * g)(x, y, z)) = (h * g)(x, y, z) - f(x, y, z)\log((h * g)(x, y, z))$. Here, $\arg\min_g$ represents the minimization with g as the variable of minimization. The form of $D(x, y, z)$ obtained using Poisson noise model makes the computational problem more complex and methods that use such form of $D(x, y, z)$ typically use simplified forms[9–13] for the prior $p(g)$. The recent trend is to assume Gaussian noise model to reduce the complexity of $D(x, y, z)$ and increase the complexity of $J(g)$, which has been found to be more rewarding in terms of output image resolution. We will also restrict to this type of approach in the remainder of the article.

The quality of restoration in such methods is determined mainly by the nature of the roughness functional used. A roughness functional is typically composed of magnitude of the image derivatives of chosen order. Two types of such functionals have been used so far

$$J_1(g) = \sum_x \phi\left(\sum_{i=1}^{3} \left(\frac{\partial}{\partial x_i} g(\mathbf{x}) \right)^2 \right), \qquad (9)$$

$$J_2(g) = \sum_x \phi\left(\sum_{j=1}^{3} \sum_{i=1}^{3} \left(\frac{\partial}{\partial x_j} \frac{\partial}{\partial x_i} g(\mathbf{x}) \right)^2 \right). \qquad (10)$$

Here ϕ is the so-called potential function that determines how high derivative values should be penalized. Here, we have used an alternative notation $\mathbf{x} = (x_1, x_2, x_3)$ to represent a 3D pixel location. Since noise adds roughness to the images, minimizing derivatives effectively removes noise. However, since fine details of image structure will also contribute to high-derivative magnitude, image details will also be lost, especially when λ is set high to cope-up with the noise. Interestingly however, the choice of ϕ determines the extent to which the image details are lost.

When the function is ϕ identity, then the functionals J_1 and J_2 are quadratic. If positivity is not enforced, they give solution in a single step. However, they give over-smoothed results. A well-known quadratic regularized method is the Tikhonov filtering. A variant of Tikhonov filtering adopted for microscopy by adding positivity constraint is known as iterative constrained Tikhonov–Miller method, which is widely used in practice[14]. However, this method gives low-resolution results when the noise is high. When $\phi(\cdot) = \sqrt{\cdot}$, the functionals J_1 and J_2 are known as total variation functionals. Methods that use J_1 with $\phi(\cdot) = \sqrt{\cdot}$ are called first-order total variation (TV) methods and the ones that use J_2 with $\phi(\cdot) = \sqrt{\cdot}$ are

known as the second-order TV methods. These methods give better resolution when compared to quadratic methods. Even though there is no theoretical proof for their superiority, it is generally believed that their improved performance stems from the fact that the weaker penalty of minimizing the absolute value allows some high derivative points, whereas quadratic minimization tends to forbid high derivative points. these methods are however computationally expensive. Initially the focus in the literature was using the first-order TV[15–17]. The main problem in using the first-order TV is that it gives solution that is composed of piece-wise constants when λ is set high to accommodate high level of noise. Recently, researchers have started focusing on using second-order TV to avoid this problem. It has been reported by several authors that using second-order TV gives much better resolution without the problem of piece-wise constants mainly using 2D deconvolution examples. Only recently, second-order TV has been successfully applied for 3D deconvolution for microscopy[18].

There are some variants of the total variation method formulated for other inverse problems, that use, in order to facilitate minimization, a different kind of ϕ. They are known as half-quadratic regularized methods and are 'functionally' equivalent to total variation methods[19–21]. There is another class of methods that uses sum of absolute values of wavelet coefficient as the regularization functional, and the optimization is performed in the wavelet domain, i.e. the wavelet coefficients are treated as the variables of minimization. The main advantage in this formulation is that no explicit derivative is necessary for noise suppression because the wavelet transform itself has inbuilt multiresolution derivatives with the order of derivative determined by the nature of the wavelet function used. As a result, since the regularization does not cause any interaction between the variables of minimization, this class of methods has a better numerical behaviour[22,23]. Nevertheless, the computational problem is still complex for real-world image sizes, and there is only one available practical implementation in this category that works on 3D volumes, which is based on an innovative iterative minimization technique[24,25]. These methods, however, give artefacts due to the fact that wavelet transforms are not invariant to rotations.

The improvement obtained by applying an efficient deconvolution method on the images measured by an widefield microscope is twofold: (i) it recovers low Fourier frequencies in the missing cone region of the OTF and (ii) it re-emphasizes the Fourier frequencies that were passed by the OTF with high attenuation. Both improvements are important to maximize the clarity of fine details in the image. We will use the term 'effective resolution' qualitatively to denote the clarity of fine details of the images after deconvolution. The effective resolution degrades with noise level, and the efficiency of the deconvolution determines the extent of degradation.

Widefield microscopy in 4D: phototoxicity and effective resolution

When a live cell is subject to fluorescence imaging, it gets damaged in two ways. The first type of damage, which may occur in any type of light microscopes, is caused by irradiation by the high-intensity illumination light that causes damage by breaking down the chemical bonds. This type of damage can be eliminated by setting the illumination intensity at sufficiently low levels. The second type of damage occurs only in fluorescence microscopy. This is due the fact that fluorophore, when in excited state, reacts with molecular oxygen and generates free radicals that react with proteins leading to damage to the cell. While the first type of damage can be avoided by setting the illumination intensity sufficiently low, the second type of damage occurs even at the intensity that is considered to be low by the live cell imaging community. Also, the effect of this type of damage gets accumulated over the imaging duration. This means that the excitation dose (product of illumination intensity and duration of exposure per 2D image measurement) should be kept as low as possible when imaging in 4D, since it requires acquiring large number of 2D images to ensure sufficient sampling in both z and t axes. Hence the difference between the effective spatial resolution and the theoretical spatial resolution is much higher in 4D imaging than in 3D imaging. This is true even in the case of widefield microscopy, despite the fact that it is the most economical in the sense of giving highest SNR for a given excitation dose.

To understand how the effective resolution degrades with reduction in the excitation dose, Figure 5 displays widefield images of immobilized yeast vacuole obtained with different excitation dose levels. The figure shows eight pair of images, where in each pair the top image is an xy section and the bottom image is an xz section. Each of the four rows displays images obtained from a specific excitation dose level relative to the highest dose level. The first column gives the raw images and the second column gives images deconvolved using a popular commercial software known as Huygens. The images clearly demonstrate how reduction in excitation dose degrades the effective resolution.

With reference to Figure 5, it turns out that noise levels in images corresponding to excitation dose level 1.5% indeed correspond to realistic experimental scenarios in live cell imaging. In a recent study involving viability of yeast cells undergoing widefield fluorescence imaging[26], the authors report that safe illumination dose levels are at least 1000 times lower than what is typically considered to be low. In particular, it turns out that in imaging yeast cells for a complete cell cycle with sufficient time sampling rate, the noise level corresponding to the dose level that does not affect the viability is comparable to the noise levels in the images of Figure 5 d. For such noise

levels, the effective resolution is too low to allow quantitative visualization of subcellular structures.

To demonstrate this problem with another example, Figure 6 shows raw and deconvolved images of a yeast synaptonemal complex (SC). This is the structure that forms between homologous chromosomes during meiosis and is believed to promote reciprocal exchange of DNA between homologous chromosomes. A protein in the SC known as Zip1, mediates key events in synapsis, crossing over and the segregation of chromosomes. Zip1 appears as filaments when viewed within the resolution limit of 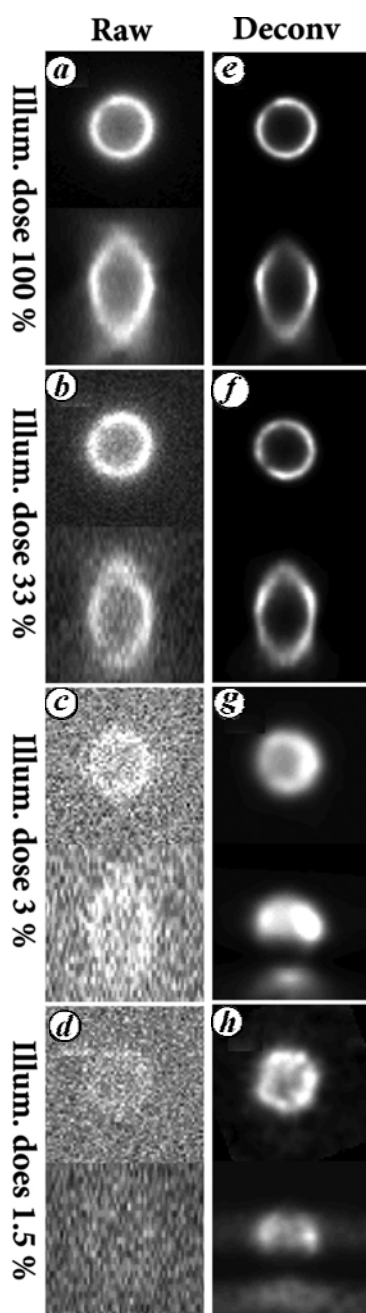optical microscopes. The images show these filaments labelled with green fluorescence protein. Figure 6 a shows the raw image and Figure 6 b shows the image obtained by applying the deconvolution method by Lefkimmiatis et al.[18], which we consider as one of the latest advancements. We postpone the interpretation of Figure 6 c till the next section. Clearly, resolution of both raw image and the image deconvolved by the method of Lefkimmiatis et al.[18] is inadequate to understand the exact topological changes that the filaments undergo. It should be emphasized that the excitation dose level used in measuring the raw images in Figure 6 is still higher than the tolerable level reported by Carlton et al.[26].

This implies that according to current status of the technology excluding our most recent development, there is no viable way to study live cell dynamics of yeast. This is bad news, because yeast is an excellent model organisms since its genome is simple and hence easy to manipulate. At the same time, yeasts is an eucaryote meaning that they share many important properties with human cells. Building a viable technology for 4D imaging of yeast without perturbing normal functions will lead to significant advancement in cell biology.

A recent breakthrough: adapting the regularization for fluorescence image characteristics

The main factor that limits the output resolution in deconvolution is the ability of the roughness functional to discriminate the contribution of noise to roughness against the roughness contributed by the high frequency of the signal. While it seems impossible to achieve this locally at any given image point, we have seen that quadratic and TV regularization functionals have comparable effect on the high derivative values of noise but have different effect on the high derivative values of the signal. While there is no theoretical analysis available to explain this effect, it is understood that it is mainly due the fact that the TV functional corresponds to the prior probability $p(g)$ that matches better with actual statistics of the high derivative points in images. This observation is applicable for all types of images, including fluorescence microscopy images.
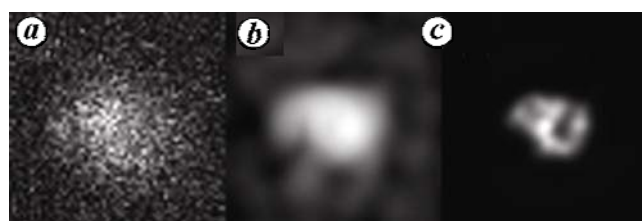

Figure 5. Effective resolution versus excitation dose.

Figure 6. *xy* cross-section of Zip1 filaments of yeast synaptonemal complex involved in yeast meiosis. *a*, Raw image; *b*, Image deconvolved using the method of Lefkimmiatis et al.[18]. *c*, Image deconvolved using our recently developed method[7]. The cross-section contains a curved filament which is clear only from the output of our method.

Fluorescence images have distinctive statistics in terms of the distribution of high derivative values mainly due to the fact that structures that are imaged are actually light sources. Surprisingly, however, there is no method that tunes $p(g)$ specifically to match characteristics of fluorescence images. In our recent work[7], we used the following observations pertaining to spatial characteristics of fluorescence images. We first observe that in fluorescence images, the percentage of points having non-negligible derivative magnitudes is much lower than that for general images. Also, among the points that have non-negligible derivative values, the ratio of high magnitude derivative points versus intermediate magnitude derivative points is much higher when compared to more generic images. Second, we also observe that high intensity points are also sparsely distributed and are co-located with high magnitude derivative points. Based on these two observations, we proposed the following roughness functional

$$J_3(g) = \sum_x \log\left(g^2(\mathbf{x}) + \sum_{j=1}^{3}\sum_{i=1}^{3}\left(\frac{\partial}{\partial x_j}\frac{\partial}{\partial x_i} g(\mathbf{x}) \right)^2 \right). \quad (11)$$

This led to a substantial improvement in the output resolution when compared to existing methods. Even though widefield deconvolution has long been a topic of research, our method is the first one designed to exploit very general spatial characteristics of fluorescence images. As a result, it is able to distinguish between the contribution of signal to the roughness and the contribution of noise to the same. Hence its output resolution differs from that of the existing methods by unusually high magnitude.

To understand how significant the improvement is, we refer to Figure 6 again. In the output of the method of Lefkimmiatis et al.[18], the loop of the Zip1 filament is seen only as a blob. On the other hand, the loop is clearly visible in the output of our method (Figure 6 c). Figure 7 gives another example to demonstrate the magnitude of the improvement obtained from our method. It shows the colour-coded z-projection of mouse nucleus labelled with GFP-tagged tetracycline repressor protein. While the output of the method of Lefkimmiatis et al.[18] does not show individual filaments, the output of our method clearly reveals individual filaments. These two examples demonstrate that our method can enable the study of dynamic cellular processes at dose levels that have never been considered practical before, thereby opening new possibilities in cell biology research. In particular, the excitation dose level used in measuring the raw images in Figure 7 is within the tolerable level for yeast cells even if imaging is performed for complete cell cycle in the sense of the study reported in ref. 26. This means that 4D imaging of yeast with adequate effective resolution for complete cell cycle is now possible using the new method.

The main issue in interpreting Figures 6 and 7 is that, since the structure is completely obscured in raw images, the validity of the structures shown in the deconvolved images of our method (Figures 6 c and 7 c) becomes questionable. In other words, it is required to demonstrate that the structures revealed by our method are not artifacts, but indeed true underlying structures. We can demonstrate this using images obtained from fixed samples with comparable noise levels. Figure 8 displays high and low dose images obtained from a fixed yeast cell expressing Zip1 filament of synaptonemal complex. The high dose was set such that the structure is clearly visible from the raw images, whereas the low dose was set such that the structure is completely obscured in the raw images.
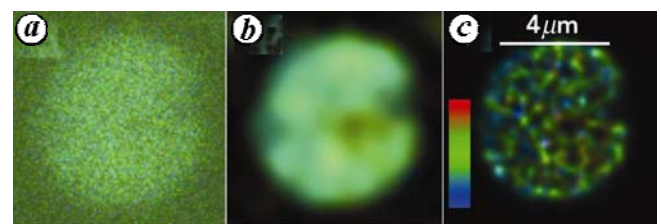

Figure 7. Colour-coded z-projections of mouse nucleus labelled with GFP-tagged tetracycline repressor. (**a**) Raw image; (**b**) Image deconvolved using the method of Lefkimmiatis et al.[18]. (**c**) Image deconvolved using our recently developed method[7]. Individual filaments are visible only in the output of our method. The colour patch in (**c**) represents how depth information is coded into colour. Red represents 2 μm depth and blue represents 5 μm depth.
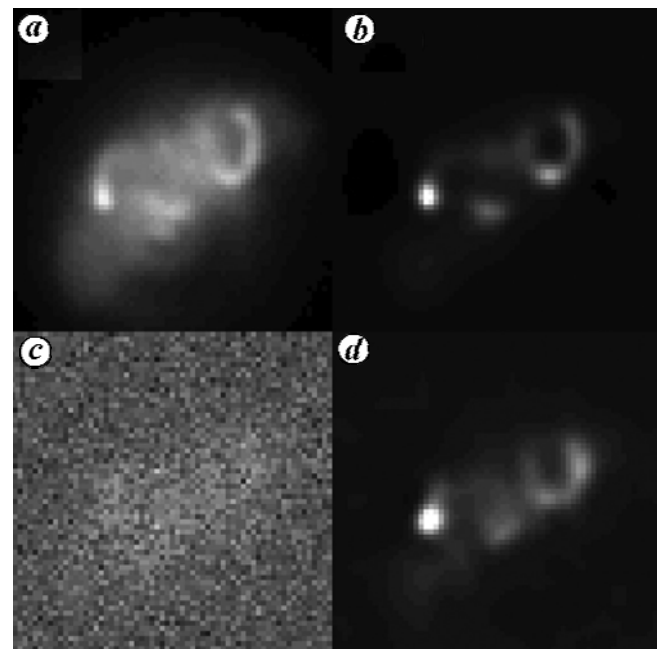

Figure 8. xy cross-section of Zip1 filaments of synaptonemal complex captured from a fixed yeast cell. (**a**) Raw image measured with high exposure; (**b**) Image deconvolved from (**a**) using our recently developed method[7]; (**c**) Raw image measured with 400 times lower exposure. (**d**) Image deconvolved from (**c**) using our recently developed method[7].

Remarkably, deconvolved images obtained from high and low dose raw images show identical structures. This demonstrate that our method can retrieve valid structures from extremely noisy images even if the structure is completely invisible. Obviously, this type of multi-exposure test cannot be done in 4D imaging since the sample will be moving. However, this can be considered as a confidence test for the validity of results presented in Figures 6 *c* and 7 *c*.

If the imaging is performed at multiple wavelengths to visualize different subcellular organelles independently, the excitation dose level corresponding the images in Figure 7 is still high enough to cause damage to yeast cells. This imposes a major limitation in cell biology research, since identifying key events in a cell cycle often will require simultaneous visualization of multiple components independently.

Approaches to further improve the effective resolution

It should be emphasized that the substantial improvement in the effective resolution reported in the previous section was due to our construction of regularization functionals based on simple qualitative observations. Here we propose few quantitative approaches to further improve the regularization functional, which might potentially make 4D imaging of light-sensitive cells at multiple wavelengths feasible.

Tuning the prior probability function to match fluorescence images

As mentioned earlier, fluorescence images have distinctive statistics in terms of the distribution of high derivative values mainly due to the fact that structures that are imaged are actually light sources. We here provide an approach to quantitatively tune the regularization functional according to the statistics of fluorescence images. To this end, we first define

$$E_0(x_1, x_2, x_3) = g^2(x_1, x_2, x_3), \tag{12}$$

$$E_k(x_1, x_2, x_3) = \sum_{i_1=1}^{3} \sum_{i_2=2}^{3} \cdots \sum_{i_k=1}^{3} \left(\frac{\partial}{\partial x_{i_1}} \frac{\partial}{\partial x_{i_2}} \cdots \frac{\partial}{\partial x_{i_k}} g(x_1, x_2, x_3) \right)^2, \tag{13}$$

and then define

$$J(g) = \sum_{x_1, x_2, x_3} \phi \left(E_0(x_1, x_2, x_3) + \sum_{j=1}^{n} \lambda_1 E_j(x_1, x_2, x_3) \right). \tag{14}$$

Now, one can optimize the parameters $\lambda_1, \ldots, \lambda_n$ and the function ϕ such that the prior probability function

$p(g) = e^{-\lambda J(g)}$ better matches spatial characteristics of fluorescence images. This can be done using a training set of high-resolution fluorescence images.

Constructing prior probability functions specific to biological experiments

In a biological experiment involving 4D fluorescence imaging, obtaining an adequate resolution is a challenge only if imaging is required to be performed for an extended period of time. This is because, in such kind of experiments, it is required to set excitation dose at very low levels to control its accumulated effect, and hence noise will be very high degrading the resolution. If it is not required to perform imaging for an extended period of time, one can set the excitation dose high so that any existing modern deconvolution method can give a sufficient resolution. We propose to use this fact to construct better prior probabilities.

For a given type live cell process, we make a population of cells such that each is at different stage of the given process. We then perform short-term 4D imaging of the cells from this population with high illumination dose such that the collection 4D images represent all stages of the live cell process. As a result, we will have captured all patterns of spatio-temporal variations of the structure to be studied using low noise images. These images can be deconvolved using any modern method and then used to build prior model as described in the previous subsection.

The resulting prior model will be a good representation of the patterns of the spatio-temporal structural variations of the given live cell process. As a result, the deconvolution method built using this prior model will give high output resolution even in the presence of unusually high levels of noise. In particular, the method can retrieve adequate resolution from 4D images obtained by setting illumination dose at very low levels, as long as images are from the same type of cellular process.

Using Langrangian derivative for discriminating roughness of a signal against noise roughness

Langrangian derivative or material derivative is the temporal derivative taken with material point fixed, whereas ordinary derivatives are taken with fixed coordinate point. At any instant and at any location, material derivative will be zero if the following conditions are met: there is no change in the fluorophore concentration in the target structure and time sampling rate is sufficiently high. On the other hand, ordinary derivatives will be zero only in those locations where there is no motion or spatial derivatives are zero. This confirms that material derivatives produce mere zeros when compared to ordinary derivatives. On the other hand, material derivatives will have

the same effect on noise, as noise has no correlation with time. This means that regularization functional built using material derivatives will have better power to discriminate the roughness of signals against the roughness of noise. As a result, the deconvolution method built using material derivatives-based regularization functionals will yield higher output resolution.

Conclusion

For a study involving 4D fluorescence microscopy, its success in analysing the spatio-temporal dynamics of a live cell process is determined by the efficiency of the deconvolution method in retrieving adequate resolution in the presence of a large amount of noise. According to the currently published literature, excluding our recently developed method[7], such studies on light-sensitive cells will be infeasible, since the low dose requirements lead to high levels of noise, which overpowers those methods causing their failure to retrieve adequate resolution. The method we developed[7] efficiently handles the levels of noise involved in such type of experiments yielding adequate resolution required for the success of the study. This was possible, because of the qualitative observations we made on the characteristics of fluorescence images, which helped to improve the form of the regularization functional. Inspired by this success, we have outlined few approaches to further improve the effective resolution of 4D microscopy which might lead to the feasibility of even newer types of experiments.

1. Rieder, C. and Khodjakov, A., Mitosis through the microscope: advances in seeing inside live dividing cells. *Science*, 2003, **4**, 91–96.
2. Fung, J., Marshall, W., Dernburg, A., Agard, D. and Sedat, J., Homologous chromosome pairing in *Drosophila melanogaster* proceeds through multiple independent initiations. *J. Cell Biol.*, 1998, **141**, 5–20.
3. Pelham, Jr. R. and Chang, F., Actin dynamics in the contractile ring during cytokinesis in fission yeast. *Nature*, 2002, **419**, 82–86.
4. Beaudouin, J., Gerlich, D., Daigle, N., Eils, R. and Ellenberg, J., Nuclear envelope breakdown proceeds by microtubule-induced tearing of the lamina. *Cell*, 2002, **108**, 83–96.
5. Moira, R., Yoona, M., Khuona, S. and Goldmana, R., Nuclear lamins a and B1: different pathways of assembly during nuclear envelope formation in living cells. *J. Cell Biol.*, 2000, **151**, 1155–1168.
6. Kumari, S. and Mayor, S., ARF1 is directly involved in dynamin-independent endocytosis. *Nature Cell Biol.*, 2008, **10**, 30–41.
7. Arigovindan, M. *et al.*, High-resolution restoration of 3D structures from extreme low SNR widefield fluorescence images. *Proc. Natl. Acad. Sci.*, Early Edition, doi: 10.1073/pnas.1315675110.
8. Jansson, P., *Deconvolution of Images and Spectra*, Academic Press, 1996, 2nd edn.
9. Lane, R., Methods for maximum-likelihood deconvolution. *J. Opt. Soc. Am. A*, 1996, **13**(10), 1992–1998.
10. Conchello, J., Enhanced 3-D reconstruction from confocal scanning microscope images. 1: Deterministic and maximum likelihood reconstructions. *Appl. Opt.*, 1990, **29**, 3795–3804.
11. Conchello, J., Kim, J. and Hansen, E., Enhanced three-dimensional reconstruction from confocal scanning microscope images. II. Depth discrimination versus signal-to-noise ratio in partically confocal images. *Appl. Opt.*, 1994, **33**(17), 3740–3750.
12. Conchello, J., Super-resolution and convergence properties of the expectation–maximization algorithm for maximum-likelihood deconvolution of incoherent images. *J. Opt. Soc. Am. A*, 1998, **15**(10), 2609–2620.
13. Conchello, J., Fluorescence photobleaching correction for expectation maximization algorithm. In *Three-Dimensional Microscopy: Image Acquisition and Processing* (eds Wilson, T. and Cogswell, C. J.), SPIE 2412-21, 1995, pp. 138–146.
14. Kempen, G., van der Voort, H., Baumen, J. and Strasters, K., Comparing maximum likelihood estimation and constrain Tikhonov–Miller restoration. *IEEE Eng. Med. Biol. Mag.*, 1996, **15**, 76–83.
15. Dey, N., Blanc-Feraud, L., Zimmer, C., Roux, P., Kam, Z., Olivo-Marin, J. and Zerubia, J., Richardson Lucy algorithm with total variation regularization for 3D confocal microscope deconvolution. *Microsc. Res. Tech.*, 2006, **69**, 260–266.
16. Hom, E., Marchis, F., Lee, T., Haase, S., Agard, D. and Sedat, J., AIDA: an adaptive image deconvolution algorithm with application to multi-frame and three-dimensional data. *J. Opt. Soc. Am. A*, 2007, **24**, 1580–1600.
17. Oliveira, J. P., Bioucas-Dias, J. M. and Figueiredo, M. A. T., Adaptive total variation image deblurring: a majorization–minimization approach. *Signal Process.*, 2009, **89**(9), 1683–1693.
18. Lefkimmiatis, S., Bourquard, A. and Unser, M., Hessian-based regularization for 3-D microscopy image restoration. Proceedings of the Ninth IEEE International Symposium Biomed Imaging: From Nano to Macro (ISBI'12), Barcelona, Spain, 2–5 May 2012, pp. 1731–1734.
19. Charbonnier, P., Blanc-Feraud, L., Aubert, G. and Barlaud, M., Deterministic edge-preserving regularization for computed imaging. *IEEE Trans. Image Process.*, 1997, **6**, 298–311.
20. Geman, D. and Yang, C., Nonlinear image recovery with half-quadratic regularization. *IEEE Trans. Image Process.*, 1995, **4**, 932–946.
21. Nikolova, M. and Ng, M., Analysis of half-quadratic minimization methods for signal and image recovery. *SIAM J. Sci. Comput.*, 2005, **27**, 937–966.
22. Figueredo, M. and Nowak, R., An EM algorithm for wavelet-based image restoration. *IEEE Trans. Image Process.*, 2003, **12**, 906–916.
23. Daubechies, I., Defrise, M. and De Mol, C., An iterative thresholding algorithm for linear inverse problems with a sparsity constraint. *Commun. Pure Appl. Math.*, 2004, **57**, 1413–1457.
24. Vonesch, C. and Unser, M., A fast thresholded Landweber algorithm for wavelet-regularized multidimensional deconvolution. *IEEE Trans. Image Process.*, 2008, **17**, 539–549.
25. Vonesch, C. and Unser, M., A fast multilevel algorithm for wavelet-regularized image restoration. *IEEE Trans. Image Process.*, 2009, **18**, 509–523.
26. Carlton, P. *et al.*, Fast live simultaneous multi-wavelength four-dimensional optical microscopy. *Proc. Natl. Acad. Sci. USA*, 2010, 1004037107v1-7.